

Intrinsic and Extrinsic Factors Influencing the Dynamics of VO₂ Mott Oscillators

Stephanie M. Bohaichuk^{1,*}, Suhas Kumar^{2,†}, Mahnaz Islam¹, Miguel Muñoz Rojo^{1,3}, R. Stanley Williams⁴, Gregory Pitner¹, Jaewoo Jeong⁵, Mahesh G. Samant⁵, Stuart S.P. Parkin^{1,5}, and Eric Pop^{1,6}

¹Department of Electrical Engineering, Stanford University, Stanford, California, USA

²Sandia National Laboratories, Livermore, California, USA

³Department of Thermal and Fluid Engineering, University of Twente, Enschede, Netherlands

⁴Department of Electrical & Computer Engineering, Texas A&M University, College Station, Texas, USA

⁵IBM Almaden Research Center, San Jose, California, USA

⁶Department of Materials Science and Engineering, Stanford University, Stanford, California, USA



(Received 4 September 2022; accepted 30 January 2023; published 10 April 2023)

Oscillatory devices have recently attracted significant interest as key components of computing systems based on biomimetic neuronal spiking. An understanding of the time scales underlying the spiking is essential for engineering fast, controllable, low-energy devices. However, we find that the intrinsic dynamics of these devices is difficult to properly characterize, as they can be heavily influenced by the external circuitry used to measure them. Here we demonstrate these challenges using a VO₂ Mott oscillator with a sub-100-nm effective size, achieved using a nanogap cut in a metallic carbon nanotube electrode. Given the nanoscale thermal volume of this device, it would be expected to exhibit rapid oscillations. However, due to external parasitics present within commonly used current sources, we see orders-of-magnitude slower dynamics. We outline methods for determining when measurements are dominated by extrinsic factors and discuss the operating conditions under which intrinsic oscillation frequencies may be observed.

DOI: 10.1103/PhysRevApplied.19.044028

I. INTRODUCTION

Brain-inspired computing has attracted much interest as a path to more efficient artificial intelligence. Hardware implementations of such systems often require fast, controllable, low-energy sources of neuronlike spiking [1,2]. Such spiking can be produced in compact memristive switches, which are two-terminal devices exhibiting electronic instabilities like negative differential resistance (NDR), often constructed using channel-forming oxides [3], chalcogenides [4], or Mott insulators that undergo an insulator-metal transition (IMT) [5–7]. Examples of Mott insulators include vanadium dioxide (VO₂) and niobium dioxide (NbO₂), which undergo an IMT at around 340 K and 1070 K, respectively. As the temperature is increased above this IMT temperature, the material undergoes an abrupt increase in conductivity, typically by several orders of magnitude, which reverses upon cooling.

Devices constructed from such switching materials frequently exhibit strong coupling between nonlinear thermally-activated electrical transport and localized Joule heating [8,9]. When measured using a voltage source,

feedback between these processes leads to abrupt volatile switching in current and resistance, but when a device is driven by a current source, it displays an electronic instability and NDR. When biased within the region of NDR in the presence of one or more parallel capacitors, the volatile resistive switching of the device, together with the parallel capacitor's charging and discharging, can produce periodic self-sustained oscillations in the device voltage and current. This setup is known as a relaxation oscillator or a Pearson-Anson oscillator, and can produce sharp spiking, useful in the construction of biomimetic circuits [10–16]. The parallel capacitor involved in excitations can originate from intrinsic device capacitance, unintended external parasitics, or intentionally added external capacitor(s). Identifying which of these capacitances are driving the dynamics and influencing the oscillation frequency can be challenging, especially because current source instabilities can complicate measurements of oscillations. Consequently, the resulting oscillation frequencies can be incorrectly assigned to the device's intrinsic thermal and electrical time scales.

In this work, we probe the IMT in sub-100-nm regions of VO₂ using a nanogap cut in a single-wall metallic carbon nanotube (CNT), which forms ultranarrow electrodes approximately 1 nm in diameter. This nanogap

*sbohaichuk@alumni.stanford.edu

†su1@alumni.stanford.edu

test platform was inspired by previous work with phase-change memory [17], but has not been applied to volatile switches until now. We expect that an increase in oscillation frequency and reduction in energy might be gained by shrinking Mott switches down to the nanoscale, especially if device capacitance reduces [6,18]. However, despite the extremely small volume (low thermal mass) heated and cooled across the IMT, these nanogap devices oscillate at (kilohertz) frequencies comparable to much larger, micrometer-sized devices due to the influence of electrical capacitance from the current source. In contrast, we find that we are able to access intrinsic device dynamics in devices with a single metallic CNT used as an additional nanoscale heat source, either by reconnecting the cut CNT with metallic VO₂ at higher bias or by using a continuous CNT [19]. We address means for identifying the dominant electrical capacitance involved in oscillations as either intrinsic or extrinsic to the device. We also show that device dynamics may be effectively switched between different driving capacitors depending on the choice of the series resistor as well as electrothermal device parameters, providing a means to reconfigure spiking frequency and avoid current source interference.

II. RESULTS AND DISCUSSION

A. Nanogap device structure and characterization

As shown in Figs. 1(a) and 1(b), we fabricate nanoscale VO₂ devices by utilizing single-walled metallic CNTs approximately 1 nm in diameter as electrodes. Aligned CNTs are grown on a quartz substrate and transferred [21,22] onto a thin film (5 nm thick) of VO₂ grown epitaxially [23] on TiO₂ (101). After patterning the VO₂ by wet

etching, 50-nm-thick Pd is deposited to make metallic contacts with both the VO₂ and CNTs [22]. A CNT running between the contacts is physically cut near its midpoint by using an atomic force microscope (AFM) tip (see Sec. 1 of the Supplemental Material [24] for additional fabrication details including lithography, etching, and AFM cutting).

The current-voltage behavior of the nanogap device [Fig. 1(c), corresponding to the device in Fig. 1(b)] at lower voltages (below 8 V) is dominated by the insulating VO₂ in the nanogap, with an IMT occurring in the gap at $V_S = 8.3$ V (abrupt jump in current marked “IMT1”). Once the VO₂ in the gap becomes metallic, as V_S is increased, the now metallically connected CNT acts as a localized Joule heater (i.e., the gap in the CNT is shorted by the metallic VO₂ within). This causes a second, larger IMT (marked “IMT2”) in the VO₂ along the length of the CNT, associated with a region of NDR (seen once the voltage drop across R_S is subtracted; see Supplemental Material Fig. S2 [24]) between $V_S = 20$ V and 23.4 V, followed by an abrupt jump in current at around 23.4 V. The IMT2 behavior is similar to that observed in previous work with a continuous (uncut) CNT as the heater [22]. Switching is repeatable and similar among other CNT-VO₂ nanogap devices, although the switching voltage and magnitude of change in resistance are dependent on the nanogap length (see Secs. 2 and 4 of the Supplemental Material [24]).

To experimentally validate the nanoscale heated volume and switching region associated with each IMT in these devices, we use Kelvin probe microscopy (KPM) and scanning thermal microscopy (SThM), two scanning probe techniques with sub-100-nm spatial resolution. KPM maps the local surface potential in a biased device, and when the image is first-order flattened (i.e., by removing the average

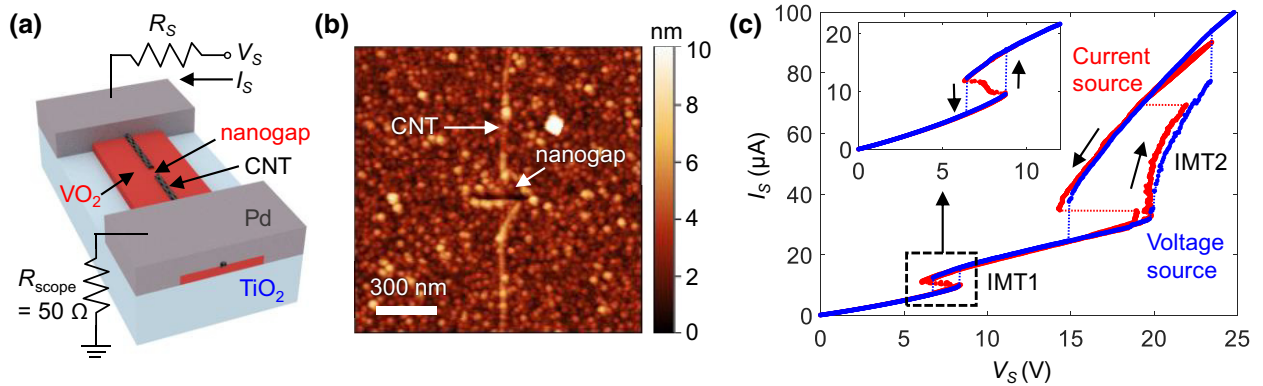


FIG. 1. CNT-VO₂ nanogap structure and static behavior. (a) Schematic illustration and measurement setup for a VO₂ device with a cut metallic CNT on top forming the electrodes. R_{scope} is the resistance of the measurement oscilloscope and $R_S = 200 \text{ k}\Omega$ is a series resistor reducing current overshoot [20] and overheating failures. (b) AFM image of a CNT on VO₂ after cutting the CNT with an AFM tip, creating a nanogap of less than 100 nm. (c) Typical quasistatic current-voltage characteristics of a nanogap device measured using a voltage source (blue) and a current source (red), showing that switching occurs in two steps. The first corresponds to the IMT of the nano-sized VO₂ volume within the CNT gap (IMT1), and the second to the larger IMT volume of VO₂ between the Pd metal contacts along the CNT (IMT2), which is connected by metallic (post-IMT1) VO₂ within the nanogap. The inset magnifies IMT1 with identical units on the axes.

linear potential drop between metal contacts; see Sec. 3 of the Supplemental Material [24]), regions of contrast highlight changes in resistance and electric field [22,25]. KPM of a nanogap device held at $V_S = 8$ V, just prior to IMT1, exhibits sharp contrast at the CNT nanogap [Fig. 2(a)], indicating a concentrated field within it.

Additionally, we use SThM to map changes in device heating [22,26], as seen on the surface of a 35-nm poly(methyl methacrylate) (PMMA) capping layer used to electrically isolate the SThM tip from the device. The same device at an identical bias imaged using SThM exhibits localized heating within the nanogap [Fig. 2(b)], while no significant heating is observed along the rest of the CNT or VO₂. This is consistent with finite-element electrothermal simulations [Fig. 2(c)] based on a thermally induced IMT in the nanogap (see Sec. 4 of the Supplemental Material [24]), which shows that significant heating occurs only in the VO₂ within the gap and at the

interface between the VO₂ and cut CNT ends. Heating at the two CNT tips forming the nanogap is dominant in the simulation, but blurring due to the finite tip size and thermal exchange radius [27] can cause the experimental appearance of a single hot spot centered on the gap. At a bias just beyond IMT1, the simulated maximum temperature of the VO₂ in the nanogap is only about 10 K above its IMT temperature ($T_{IMT} = 328$ K) in steady state.

Beyond IMT1 but prior to inducing IMT2 (at $V_S = 16$ V), much weaker contrast is observed in the flattened KPM image in Fig. 2(d), consistent with a lower voltage drop and field across the VO₂ in the gap, which turns metallic after IMT1. SThM [Fig. 2(e)] at this bias indicates that heating occurs not only in the gap, but also along the full length of the CNT, indicating that the CNT is effectively reconnected by the metallic VO₂ in the gap. Finite-element simulations shown in Fig. 2(f) also confirm

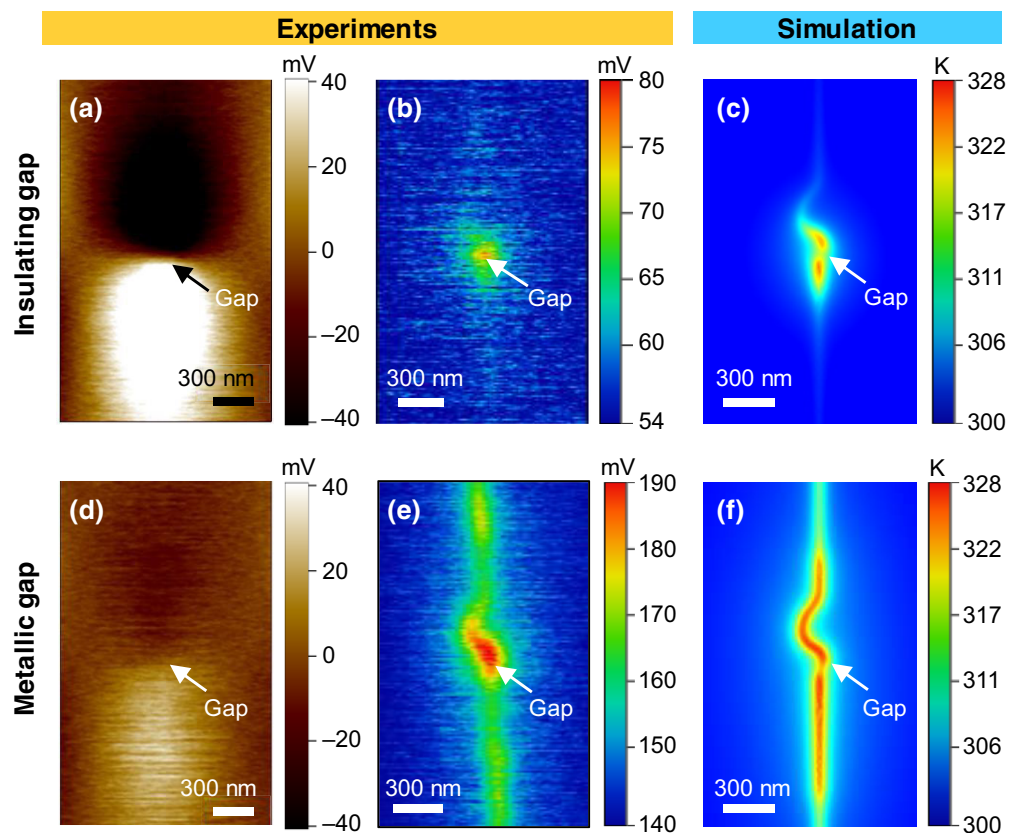


FIG. 2. Localized electric field and temperature during IMT1 and IMT2. (a) Flattened KPM image of a nanogap device held at $V_S = 8$ V (with $R_S = 200$ k Ω), just prior to IMT1. First-order flattening of the surface potential removes the average linear potential drop between the Pd contacts, and the contrast at the gap indicates a strong field within it [24]. The positive contact (ground) is outside the bottom (top) of each image. (b) SThM image of the same bias in the same device (now capped by PMMA) showing highly localized heating in the gap. The color bar refers to the SThM voltage, which is a measure of the change in local temperature on the PMMA surface. (c) Simulation of the capped nanogap device, showing the temperature on the PMMA surface prior to IMT1. (d) Flattened KPM image of the same device at $V_S = 16$ V, after IMT1 but before IMT2. There is a lower potential drop across the gap once it is metallic. (e) SThM image of the same bias and device (capped by PMMA), showing heating in the gap and also along the rest of the now-connected CNT. (f) Corresponding simulation of the capped device temperature on the PMMA surface, after IMT1.

heating of the VO₂ along the entire CNT length, leading to IMT2.

B. Origin of oscillation frequencies

When biased using a constant current within a region of NDR, it is possible to produce self-sustained periodic electrical oscillations, aided by an external or internal parallel capacitor [11,19,28]. In a comparable micrometer-scale VO₂ device made *without* a CNT ($L = 3.5 \mu\text{m}$, $W = 2.7 \mu\text{m}$) oscillations occur with a frequency of about 0.4 kHz [Fig. 3(a)], consisting of a fast initial spike of about 70 ns [inset of Fig. 3(d)] followed by a slow decay of 0.44 ms. Due to the reduced sampling rate of the oscilloscope at longer acquisition durations, the fast initial spike is not captured in Figs. 3(a) and 3(d) but is shown at shorter time scales in the inset to Fig. 3(d). In the nanogap device of Fig. 1, oscillations occur at IMT1 (corresponding to the nanogap volume) with a frequency of about

0.6 kHz [Fig. 3(b)]. A fast initial spike does not appear to be present, but only a slow decay of 1.2 ms after the IMT step. Thus, despite an enormous reduction in the volume of VO₂ heated and cooled across the IMT [observed in Figs. 2(a)–2(c)], the CNT nanogap device oscillates at nearly the same frequency as the large VO₂-only device. Similar slow oscillations are observed in other nanogap devices in IMT1 (see Sec. 2(b) of the Supplemental Material [24]).

In contrast, when the same CNT nanogap device is biased within IMT2, the CNT is reconnected as a Joule heating source (in series with the metallic VO₂ bridging the gap) and oscillations are observed to be over 1000 times faster with a frequency of 0.65 MHz [Figs. 3(c) and 3(f)]. This observation is surprising if oscillations are set solely by intrinsic electrical and thermal time constants because the volume for the IMT2 “connected nanogap” is much larger than for the IMT1 nanogap (evidenced by Fig. 2), and a larger volume usually implies slower dynamics. Yet, the IMT2 connected nanogap appears orders of magnitude

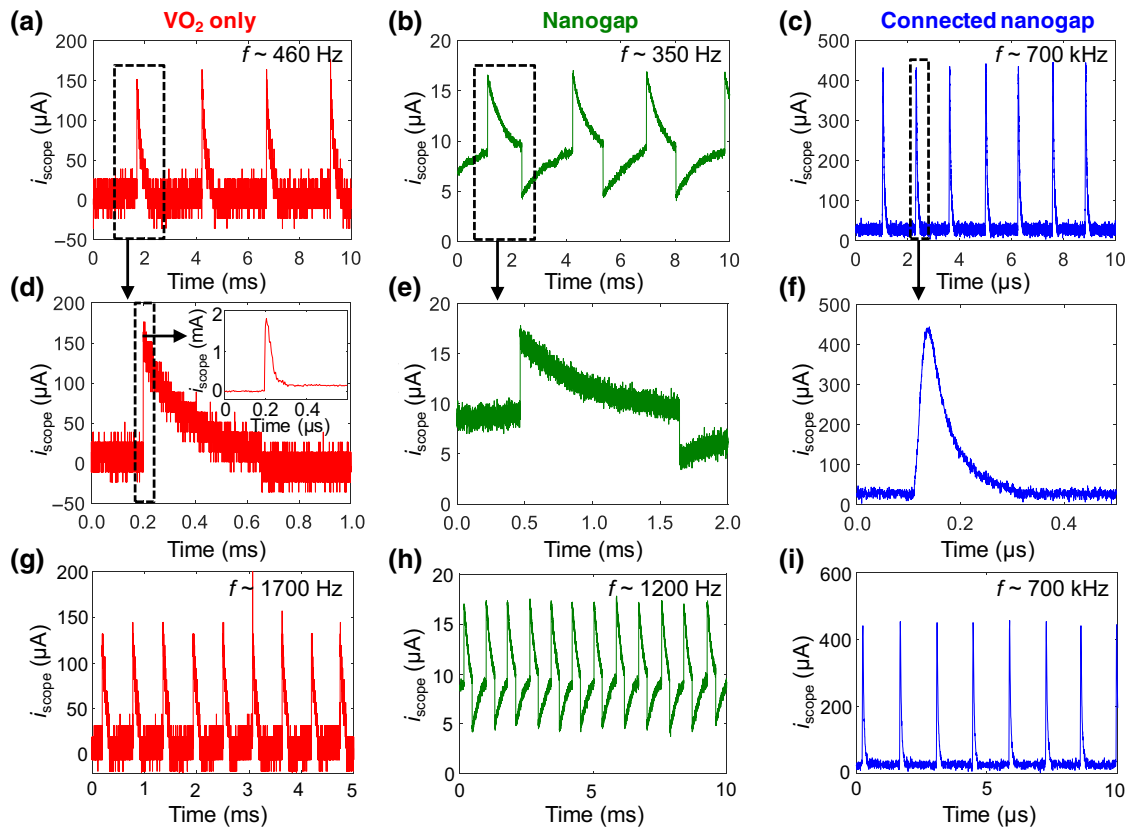


FIG. 3. Dynamics in VO₂ devices with and without a nanogap. Oscillations are measured with a 50Ω oscilloscope in series, when the device is biased with a constant current in a region of negative differential resistance (NDR). (a) A micrometer-scale VO₂ device ($L = 3.5 \mu\text{m}$, $W = 2.7 \mu\text{m}$) without a CNT, corresponding to oscillations of a large volume of VO₂. (b) A CNT nanogap device biased in IMT1, corresponding to oscillations of a nanoscale volume of VO₂ in the gap ($L_{\text{gap}} < 100 \text{ nm}$). (c) A CNT nanogap device biased in IMT2, corresponding to oscillations of VO₂ in a narrow region below the CNT, but extending along its full length ($L = 3.4 \mu\text{m}$). Despite the larger volume heated and cooled across the IMT, the VO₂ during IMT2 oscillates around 1000 times faster than in IMT1. (d)–(f) are magnified plots of (a)–(c). (g)–(h) With the same setup and devices, but with the current bias applied using a Keithley 2450 instead of a Keithley 4200-SCS source, nearly an order-of-magnitude change in oscillation frequency is produced for the VO₂ and nanogap devices operated in IMT1. (i) The nanogap device in IMT2 is not affected by a change of the current source.

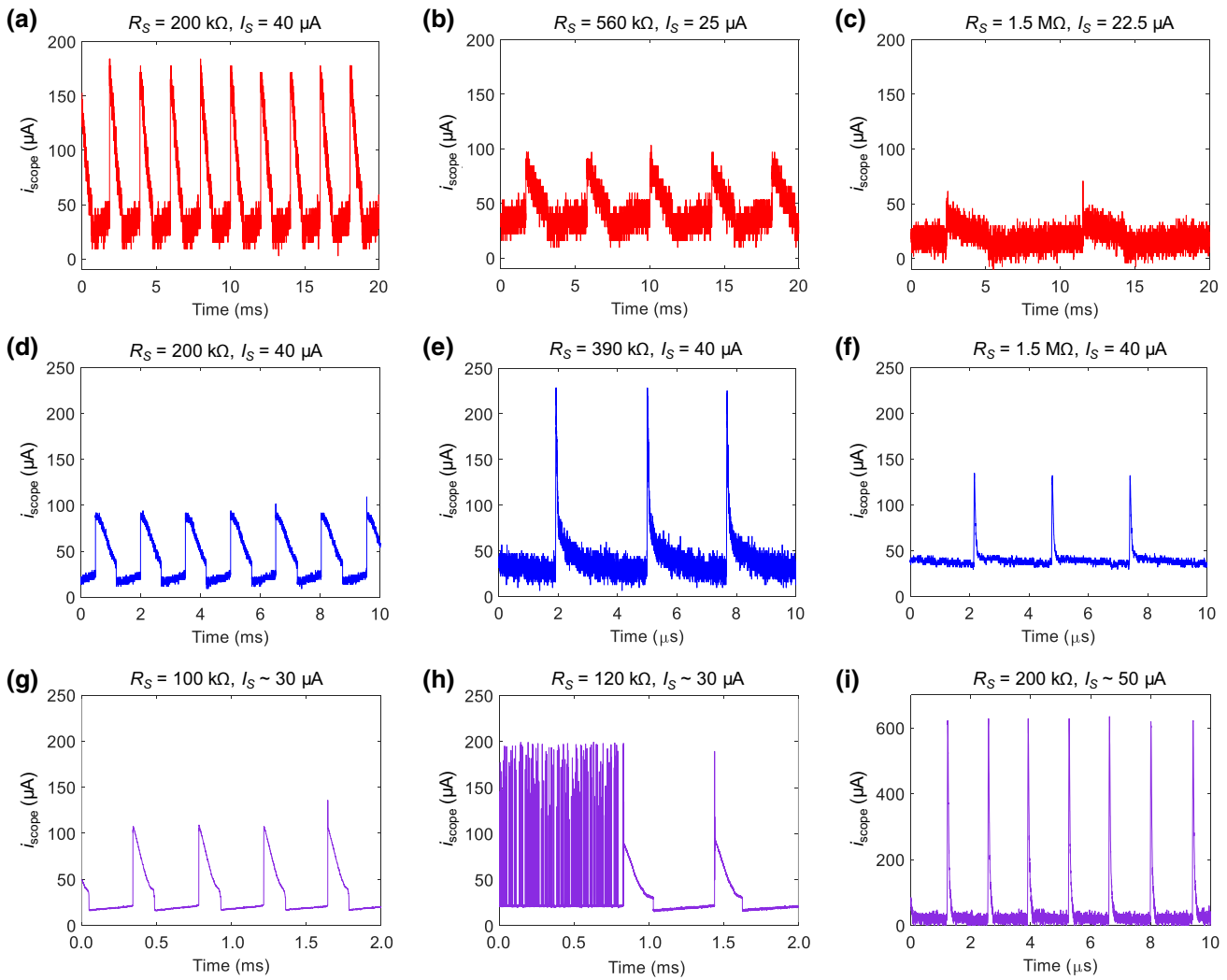


FIG. 4. Effect of the series resistor (R_S) on oscillations. (a)–(c) A micrometer-scale VO₂ device ($L \sim 5 \mu\text{m}$, $W \sim 5 \mu\text{m}$) without a metallic CNT. (d)–(f) A CNT nanogap device biased in IMT2 ($L = 4.7 \mu\text{m}$). (g)–(i) A VO₂ device with a continuous CNT heater ($L = 3.7 \mu\text{m}$). For data acquired on long (millisecond) time scales [in (a)–(d), (g),(h)], the fast rising edge spike is not displayed or is subsampled by the oscilloscope to show a smaller amplitude.

faster. This means that within the same nanogap device's effective circuit, we observe two distinct oscillation frequencies (i.e., that of IMT1 and that of IMT2) three orders of magnitude apart using a current bias differing by less than an order of magnitude.

However, these two oscillation frequencies do not represent two distinct intrinsic device time scales. Rather than being set solely by device size and thermal mass, the spiking frequency of IMT devices can be influenced by electrical capacitances, not only as part of the device contacts or geometry, but also externally from the probe station or current source itself. In our measurements, we observe that, all else being the same (namely, the bias current, cables, series resistor, probes, and the device itself), the choice of current source has a significant impact on the frequency of slow oscillations in a VO₂ device without a

CNT [Fig. 3(g)] or a nanogap device in IMT1 [Fig. 3(h)]. In these devices, the use of a Keithley 2450 SourceMeter instead of a Keithley 4200-SCS parameter analyzer to apply the same fixed current results in nearly an order-of-magnitude increase in oscillation frequency. Similarly, increases in current output range settings of either source result in significant slowing of the observed oscillations, even though the same current bias is applied. This appears to arise from changes in effective source capacitance (or other internal instabilities) with source settings, as further explored in Sec. 2(c) and Fig. S7 of the Supplemental Material [24].

In contrast, the faster oscillations of VO₂ devices with a continuous CNT heater [19] and nanogap devices in IMT2 [Fig. 3(i)] are insensitive to, and isolated from, the choice of the current source and its measurement range.

We note that in these megahertz devices, unlike the slow sub-kilohertz ones, oscillations are easily accessible using either a voltage bias (combined with an appropriate value of R_S) or a current bias. The faster frequencies thus appear to be more representative of the device's intrinsic electrical and thermal time scales.

If the changes in total resistance and voltage seen by the current source are small enough, then it may be possible to avoid significantly discharging source capacitors and involving them in the oscillations. Thus, we investigate the effects of changing the series resistor: a large R_S should more effectively isolate the system from external parasitics, while a small R_S should encourage slow oscillations. In large micrometer-sized VO₂ devices [Figs. 4(a)–4(c)], an increase in R_S has minimal impact on oscillation frequency and makes the oscillatory regime occur over a narrower range of currents so it is increasingly hard to access. No fast oscillations are observed for $200 \text{ k}\Omega \leq R_S \leq 1.5 \text{ M}\Omega$, and no stable oscillations are accessible above about $2 \text{ M}\Omega$.

As R_S increases, the amplitude of source-driven oscillations in device current generally decreases because the difference in total circuit resistance between insulating ($R_S + R_{\text{VO}_2,\text{ins}}$) and metallic states ($R_S + R_{\text{VO}_2,\text{met}} \approx R_S$) reduces. For the nanogap devices undergoing IMT1, this makes it difficult to resolve oscillations above the noise floor with larger R_S , especially because these devices have a very small change in resistance during IMT1 even before insertion of R_S .

At small values of R_S , we observe that nanogap devices in IMT2 and continuous CNT heater devices, which behave similarly and are displayed in Figs. 4(d)–4(i), show slow sub-kilohertz oscillations. These oscillations have a similar nature to VO₂ devices without a CNT, and nanogap devices in IMT1, in which the external capacitance is highly influential and sets the effective oscillation frequency. However, the nanogap IMT2 and continuous CNT devices show orders-of-magnitude faster oscillations once shielded from source parasitics at larger R_S . In this regime, the changes to the total circuit resistance ($R_S + R_{\text{device}}$) are smaller and occur over faster time scales than the source and its capacitor can track, resulting in a constant current bias to the device. Further increases to R_S do not significantly alter oscillation frequency. If a critical value of R_S is chosen, the device can become unstable and abruptly switch between fast (megahertz) and slow (kilohertz) oscillations, shown in Fig. 4(h). That is, there does not appear to be a gradual change in oscillation frequency from slow to fast as R_S is tuned, but rather two discrete frequencies.

It remains unclear as to why our micrometer-sized VO₂ devices do not exhibit rapid device dynamics at higher R_S , although this may be related to the form of the NDR and the resistance of the high-current-density channel

(metallic state) relative to the surrounding low-current-density (insulating state) VO₂ [29]. The isolation of high-speed internal dynamics in devices with a CNT heater (i.e., a connected nanogap or continuous CNT) has likely been made easier via a decrease in the device's resistance combined with changes to its electrical response to temperature, that is, on the creation and dissolution of the narrow metallic VO₂ conducting channel, and therefore its NDR and associated dynamics. This is discussed as a possibility in Secs. 2(c) and 5 of the Supplemental Material [24], but requires further study.

We find the influence of the source on device oscillation frequency to be a very common issue with measurements made using a fixed current bias, including with commonly used parameter analyzers in research laboratories such as the Agilent B1500 and the Keithley 4200. If oscillation time scales truly originate from the device, then no changes should be observed with the current source (along with associated parasitic capacitances) or its range settings, in addition to increases in the series resistor.

C. Compact modeling of factors influencing oscillation frequency

To gain further insight into the origin of oscillation time scales, we construct a compact model in which oscillations arise from a thermally driven NDR coupled to one of two electrical capacitances: one intrinsic to the device structure, and one within the current source. Furthermore, we show that the circuit dynamics can abruptly switch between excitation of each capacitor, as shown in Fig. 4(h), as a function of an electrical and/or a thermal tuning parameter, such as the external series resistor, the device thermal capacitance, and/or the strength of an added heat source like a CNT.

The device model consists of nonlinear thermally activated Schottky transport for the device [30], coupled to Newton's law of cooling [Eq. (1)], which describes the competition between self-heating and heat loss to the environment. C_{th} is the thermal capacitance (which scales with switching volume), R_{th} is a lumped thermal resistance between the hot device and the environment, T represents an average device temperature, and T_0 is the ambient temperature. i_m and v_m are the current through and voltage across the device, respectively. We examine the effect of scaling C_{th} , as well as the effect of including a resistive heater (R_{heater}), such as the CNT which appears electrically in parallel to the oscillating VO₂ biased at IMT2. This heater adds a Joule heat source term in the thermal dynamics, given as the last term of the following equation:

$$C_{\text{th}} \frac{dT}{dt} = i_m v_m - \frac{T - T_0}{R_{\text{th}}} + \frac{v_m^2}{R_{\text{heater}}} \quad (1)$$

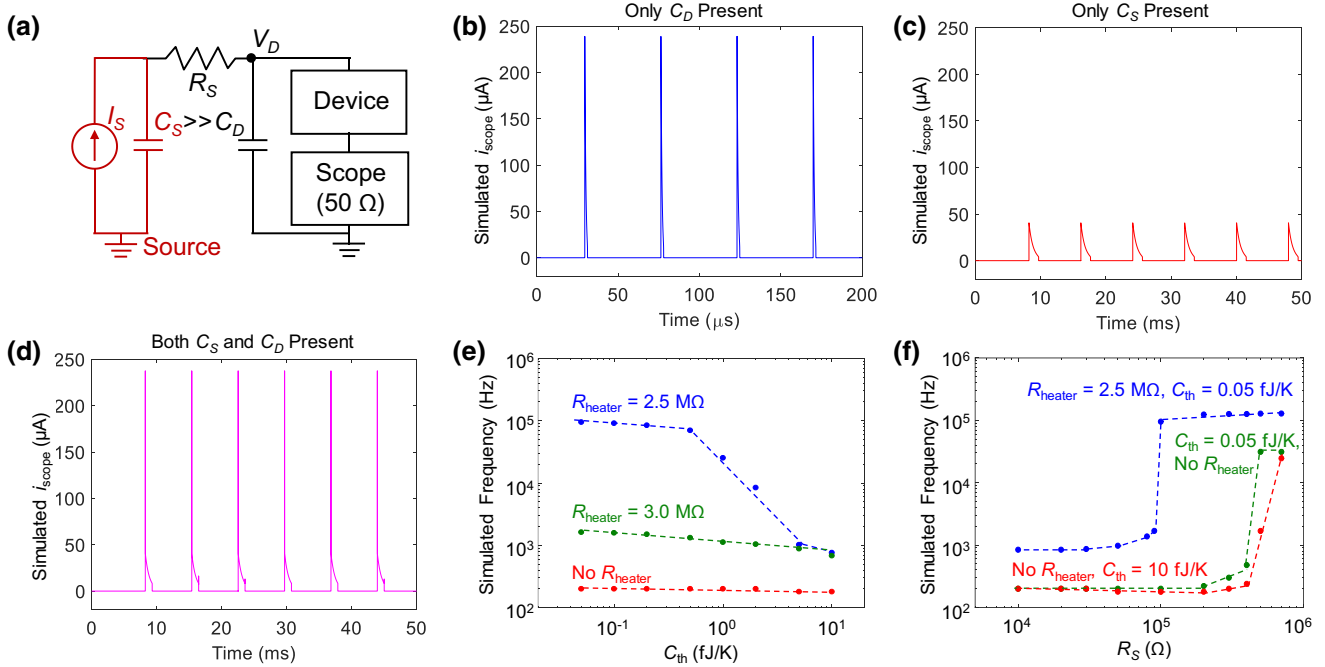


FIG. 5. Modeling of oscillations in a device with a nonlinear thermally driven instability. (a) Schematic of the simulated circuit, including a capacitance C_S associated with external parasitics (i.e., the current source), and a capacitance C_D associated with the device. When held at $I_S = 3\ \mu\text{A}$, within a region of NDR, oscillations occur (b) relatively rapidly at around 20 kHz with only C_D present, (c) relatively slowly at around 0.1 kHz with only C_S present, and (d) relatively slowly when both capacitors are in the system. In all three cases, $R_S = 100\ \text{k}\Omega$ and $C_{\text{th}} = 0.05\ \text{fJ/K}$, corresponding to a small device volume. (e) Adding a heater with resistance less than $2.5\ \text{M}\Omega$ and simultaneously reducing C_{th} produces an abrupt frequency increase (blue) by avoiding involvement of C_S . If the device only self-heats (red) or a weaker heater is used (green), then C_{th} has no effect on frequency. (f) Increasing R_S can also abruptly decouple the device dynamics from C_S , allowing a speed-up by a factor of more than 100. Adding a heater shifts the critical crossover point to lower R_S .

This nonlinear dynamical model produces abrupt resistive switching during a dc voltage sweep (due to positive feedback and thermal runaway) and an NDR instability during a current sweep, similar to IMT switching devices. The model approximates the device behavior with mathematically simple Schottky transport, as any sufficiently nonlinear thermal transport will produce volatile switching and NDR (and the associated self-oscillations in a relaxation circuit), although it does not capture all the underlying physics. We do not include an explicit IMT mechanism, instead capturing the switching and NDR with a simpler model to more clearly isolate the effects of electrical capacitance and tuning parameters that lead to dramatic changes in the dynamics.

The switching device model is incorporated into a relaxation oscillator circuit including two capacitors and a series resistor R_S , shown in Fig. 5(a). C_D represents intrinsic device capacitance, whereas C_S represents larger external parasitics like those from a current source or another device in a network. Section 5 of the Supplemental Material includes additional details, as well as an alternative configuration where C_S is instead located as a second large device capacitance [24]. When only $C_D = 30\ \text{pF}$ is present, the system oscillates rapidly at around 20 kHz for

fixed $I_S = 3\ \mu\text{A}$ (held within the region of NDR), shown in Fig. 5(b). When only a large external parasitic $C_S = 5\ \text{nF}$ is present in the system, with fixed $I_S = 3\ \mu\text{A}$, oscillations occur slowly at 0.1 kHz [Fig. 5(c)]. If both capacitors are present, then C_S dominates, resulting in low-frequency oscillations in which an initial fast spike is added to the rising edge of each slow spike, shown in Fig. 5(d). The shape of the spikes combines aspects of each electrical time scale, reproducing the behavior of our micrometer-scale VO₂ devices shown in Fig. 3(d).

The difference in duration of the rapidly decaying metallic state (the short spike) compared to the longer insulating state (between spikes) in this model (i.e., the spike spacing) stems largely from the electrical capacitance. When the device is insulating and highly resistive, any electrical time scales are large, and the capacitor charging is slow. With the rapid change in voltage upon switching, the capacitor(s) can more rapidly discharge through the much more conductive metallic device, which then cools quickly. However, we refrain from assigning a single fixed electrical or thermal time constant to either the metallic or insulating state because the device's resistance and heating change considerably throughout the dynamics. For instance, the switching speed of VO₂ is known to vary by

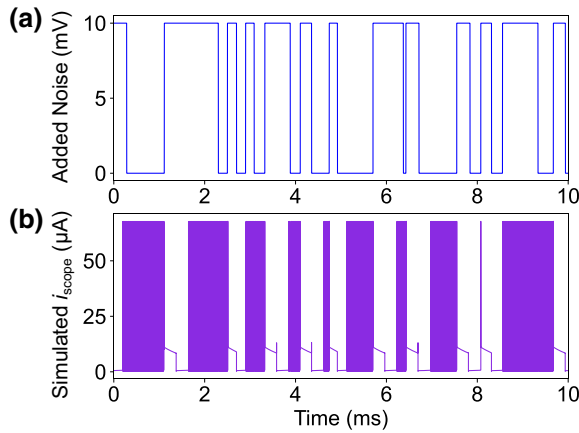


FIG. 6. Modeling of autonomous frequency jumping. Random telegraph noise is added to the device voltage with a 10-mV amplitude and millisecond time scale (upper panel). As a result, the system abruptly jumps between fast and slow oscillations (lower panel). $R_S = 95 \text{ k}\Omega$, $I_S = 5 \mu\text{A}$, $C_{\text{th}} = 0.05 \text{ fJ/K}$.

orders of magnitude depending on the applied voltage (see, for example, incubation curves in Ref. [8] and Fig. S13 in the Supplemental Material [24]), even in a purely thermal simulation with no electrical capacitance. Thus, the long spike spacing is expected to be shorter if the power in the device can be more rapidly increased by reducing electrical capacitance (if limited by an intrinsic C_D , then scaling the device could reduce this), increasing the bias setpoint, or by thermally engineering the device to heat up more for a given input power.

Preventing the larger capacitor from charging and discharging can significantly increase oscillation speed and reduce spike energy. Therefore, we investigate whether certain parameters in our model can alter which of the capacitances dominates the system's dynamics if the large capacitor C_S cannot be removed. To simulate the reduction of switching volume from micrometers to tens of nanometers, we reduce C_{th} by a factor of 1000, but find that the oscillation frequency remains nearly the same [Fig. 5(e)]. Similarly, reducing C_D has no effect on the overall oscillation frequency when C_S remains much larger. As a result, simply scaling the device is likely not enough to speed up oscillations if it does not simultaneously reduce the dominant circuit capacitance.

Instead, adding a sufficiently conductive Joule heater is found to excite C_D and avoid significant cycling of the charge on C_S , producing oscillations up to about 0.1 MHz once C_{th} is sufficiently small, as shown in Fig. 5(e). When the Joule heater is either absent or insufficiently strong, the oscillation frequency remains slow over a large range of C_{th} [Fig. 5(e)]. The combination of small thermal capacitance and an added heat source may make it easier to access faster intrinsic dynamical behavior over those dominated by large external capacitance, as in our nanogap IMT2 devices utilizing a CNT heater.

In addition, we examine the effects of the external series resistor R_S on oscillation frequency. As shown in Fig. 5(f), if R_S is too small then C_S couples into the device dynamics and produces slow sub-kilohertz oscillations. Once R_S is large enough, faster intrinsic dynamics from the interaction with device capacitance C_D are accessible. The transition between the two regimes can be abrupt, with no intermediate oscillation frequency, as is observed in our experiments. Changing C_{th} (such as through device scaling) has minimal effect, but the addition of a heat source R_{heater} pushes the critical value of R_S needed to shift to the faster sub-megahertz oscillation regime to a lower value, making it easier to produce fast spiking in the system.

Thus, a two-capacitor model can reasonably reproduce the time scales and pulse shapes observed in the experiments. The modeling results show that volume scaling can be important for achieving faster oscillations by determining C_{th} and C_D , but should be accompanied by careful control of all circuit capacitances. We find that the largest circuit capacitance, in this case external source capacitance, tends to dominate oscillatory dynamics but does not necessarily do so under all conditions. A means for probing intrinsic oscillations may be provided via the external circuitry (i.e., the series resistor), or by modifying the thermal behavior of the device itself (e.g., using a linear heater), which can change the NDR dynamics involved in oscillations.

D. Compact modeling of frequency hopping

Finally, we demonstrate that the simulated system can autonomously jump between two oscillation frequencies, observed experimentally in Fig. 4(h), when random telegraph noise (RTN) is introduced to the model. Figure 6(a) shows an example of RTN added to the device voltage [V_D in Fig. 5(a)], with amplitude 10 mV and a time scale of the order of 1 ms. This could represent noise arising from the device resistance or capacitance, such as from traps in either the CNT or the VO₂ [31,32], or perhaps from stochastic switching of small VO₂ domains (e.g., from percolation at the edges of the metallic VO₂ region or from defects with a different local T_{IMT}) [33,34]. When the system is operated in the presence of RTN with R_S near the crossover value at 95 kΩ in Fig. 5(f), oscillations repeatedly hop between the two frequencies, as shown in Fig. 6(b). Without RTN the system oscillates rapidly, but when the voltage V_D suddenly increases the system switches to slow oscillations, at least temporarily. At values of R_S far from the crossover value, here below about 80 kΩ or above about 110 kΩ, the system is unaffected by the RTN and oscillates uniformly slowly or rapidly.

Frequency hopping is observed using very small RTN amplitudes, less than 1% of the voltage V_D , and is still observed at amplitudes below 0.5 mV. As the noise amplitude reduces, the range of R_S values over which hopping is

observed shrinks, while at larger noise amplitudes fluctuations in the frequency within the slow or fast oscillations begin to be visible even when hopping does not occur. In contrast, white noise will not produce any of these effects. Similar frequency hopping is observed if RTN is added to the Joule heating process, in the value of R_{heater} in Eq. (1) or to the value of R_{th} , rather than to electrical noise on V_D . Fluctuations in these resistances of less than 1% will produce hopping behavior. Such nonlinear devices are thus highly sensitive to perturbations and instabilities when operated near crossover points.

III. CONCLUSION

In conclusion, the spiking speed of a VO₂-based Mott oscillator, and the dynamical time scales of nonlinear thermally driven oscillators in general, are not strictly determined by device geometry alone. Here, we report on how different capacitors, both intrinsic and extrinsic to a device, can influence the measured time scales of oscillatory dynamics. We find that capacitance and/or instability in the current source used to bias the device can complicate measurements of oscillations, giving rise to much slower dynamics than the device is inherently capable of. Influence of a current source can be identified by changes in response to the source used, its range settings, or the external series resistor used. However, by using a larger series resistor or by thermally engineering the device dynamics, it may be possible to avoid excitation of a large external capacitor. The construction of the electrical control circuit is therefore an important consideration in establishing and controlling the dynamics of nonlinear devices, in addition to engineering the electrical and thermal time scales of the device itself.

ACKNOWLEDGMENTS

H.S. Philip Wong is gratefully acknowledged for providing technical advice. Device fabrication was performed at the Stanford Nanofabrication Facility and the Stanford Nano Shared Facilities, supported by the National Science Foundation (NSF) under award ECCS-1542152. This work was supported in part by ON Semiconductor, by the Stanford SystemX Alliance, and by the X-Grants Program of the President's Excellence Fund at Texas A&M University. S.B. and M.I. acknowledge support from the Stanford Graduate Fellowship (SGF) program, and S.B. from the NSERC Postgraduate Scholarship program. S.K. acknowledges the Laboratory Directed Research and Development program at Sandia National Laboratories, a multimission laboratory operated for the US Department of Energy (DOE)'s National Nuclear Security Administration under contract DE-NA0003525. This paper describes objective technical results and analyses. Any subjective views or opinions that might be expressed in the paper do not necessarily represent the views of the US Department of Energy

or the United States Government. R.S.W. acknowledges the X-Grants Program of the President's Excellence Fund at Texas A&M University.

-
- [1] A. Raychowdhury, A. Parihar, G. H. Smith, V. Narayanan, G. Csaba, M. Jerry, W. Porod, and S. Datta, Computing with networks of oscillatory dynamical systems, *Proc. IEEE* **107**, 73 (2019).
 - [2] D. E. Nikonov and I. A. Young, Benchmarking delay and energy of neural inference circuits, *IEEE J. Explor. Solid-State Comput. Devices Circuits* **5**, 75 (2019).
 - [3] A. A. Sharma, Y. Li, M. Skowronski, J. A. Bain, and J. A. Weldon, High-frequency TaO_x-based compact oscillators, *IEEE Trans. Electron Devices* **62**, 3857 (2015).
 - [4] A. A. Sharma, Y. Kesim, J. A. Bain, M. Skowronski, and J. A. Weldon, in *2016 Solid State Devices and Materials International Conference*, pp. 26.
 - [5] Y. Zhou and S. Ramanathan, Mott memory and neuromorphic devices, *Proc. IEEE* **103**, 1289 (2015).
 - [6] W. Yi, K. K. Tsang, S. K. Lam, X. Bai, J. A. Crowell, and E. A. Flores, Biological plausibility and stochasticity in scalable VO₂ active memristor neurons, *Nat. Commun.* **9**, 4661 (2018).
 - [7] J. L. Andrews, D. A. Santos, M. Meyyappan, R. S. Williams, and S. Banerjee, Building brain-inspired logic circuits from dynamically switchable transition-metal oxides, *Trends Chem.* **1**, 711 (2019).
 - [8] D. Li, A. A. Sharma, D. K. Gala, N. Shukla, H. Paik, S. Datta, D. G. Schlom, J. A. Bain, and M. Skowronski, Joule heating-induced metal-insulator transition in epitaxial VO₂/TiO₂ devices, *ACS Appl. Mater. Interfaces* **8**, 12908 (2016).
 - [9] S. Kumar, Z. Wang, N. Davila, N. Kumari, K. J. Norris, X. Huang, J. P. Strachan, D. Vine, A. L. D. Kilcoyne, Y. Nishi, and R. S. Williams, Physical origins of current and temperature controlled negative differential resistances in NbO₂, *Nat. Commun.* **8**, 658 (2017).
 - [10] Y. Taketa, F. Kato, M. Nitta, and M. Haradome, New oscillation phenomena in VO₂ crystals, *Appl. Phys. Lett.* **27**, 212 (1975).
 - [11] Y. W. Lee, B.-J. Kim, J.-W. Lim, S. J. Yun, S. Choi, B.-G. Chae, G. Kim, and H.-T. Kim, Metal-insulator transition-induced electrical oscillation in vanadium dioxide thin film, *Appl. Phys. Lett.* **92**, 162903 (2008).
 - [12] M. D. Pickett, G. Medeiros-Ribeiro, and R. S. Williams, A scalable neuristor built with Mott memristors, *Nat. Mater.* **12**, 114 (2013).
 - [13] M. D. Pickett and R. S. Williams, Sub-100 fJ and sub-nanosecond thermally driven threshold switching in niobium oxide crosspoint nanodevices, *Nanotechnology* **23**, 215202 (2012).
 - [14] A. Beaumont, J. Leroy, J. C. Orlianges, and A. Crunceanu, Current-induced electrical self-oscillations across out-of-plane threshold switches based on VO₂ layers integrated in crossbars geometry, *J. Appl. Phys.* **115**, 154502 (2014).
 - [15] J. Del Valle, P. Salev, Y. Kalcheim, and I. K. Schuller, A caloritronics-based Mott neuristor, *Sci. Rep.* **10**, 4292 (2020).

- [16] B. Zhao and J. Ravichandran, Low-Power Microwave Relaxation Oscillators Based on Phase-Change Oxides for Neuromorphic Computing, *Phys. Rev. Appl.* **11**, 014020 (2019).
- [17] F. Xiong, A. D. Liao, D. Estrada, and E. Pop, Low-power switching of phase-change materials with carbon nanotube electrodes, *Science* **332**, 568 (2011).
- [18] J. Lin, S. Guha, and S. Ramanathan, Vanadium dioxide circuits emulate neurological disorders, *Front. Neurosci.* **12**, 856 (2018).
- [19] S. M. Bohaichuk, S. Kumar, G. Pitner, C. J. McClellan, J. Jeong, M. G. Samant, H.-S. P. Wong, S. S. P. Parkin, R. S. Williams, and E. Pop, Fast spiking of a Mott VO₂-carbon nanotube composite device, *Nano Lett.* **19**, 6751 (2019).
- [20] H. J. Wan, P. Zhou, L. Ye, Y. Y. Lin, T. A. Tang, H. M. Wu, and M. H. Chi, In situ observation of compliance-current overshoot and its effect on resistive switching, *IEEE Electron Device Lett.* **31**, 246 (2010).
- [21] N. Patil, A. Lin, E. R. Myers, R. Koungmin, A. Badmaev, Z. Chongwu, H. S. P. Wong, and S. Mitra, Wafer-scale growth and transfer of aligned single-walled carbon nanotubes, *IEEE Trans. Nanotechnol.* **8**, 498 (2009).
- [22] S. M. Bohaichuk, M. Muñoz Rojo, G. Pitner, C. J. McClellan, F. Lian, J. Li, J. Jeong, M. G. Samant, S. S. P. Parkin, H.-S. P. Wong, and E. Pop, Localized triggering of the insulator-metal transition in VO₂ using a single carbon nanotube, *ACS Nano* **13**, 11070 (2019).
- [23] J. Jeong, N. Aetukuri, T. Graf, T. D. Schladt, M. G. Samant, and S. S. P. Parkin, Suppression of metal-insulator transition in VO₂ by electric field-induced oxygen vacancy formation, *Science* **339**, 1402 (2013).
- [24] See Supplemental Material at <http://link.aps.org/supplemental/10.1103/PhysRevApplied.19.044028> for further information about fabrication, modeling details, as well as additional electrical and scanning probe measurements.
- [25] S. Sadewasser and T. Glatzel, *Kelvin Probe Force Microscopy: Measuring and Compensating Electrostatic Forces* (Springer, Berlin, 2011).
- [26] Y. Zhang, W. Zhu, F. Hui, M. Lanza, T. Borca-Tasciuc, and M. Muñoz Rojo, A review on principles and applications of scanning thermal microscopy (SThM), *Adv. Funct. Mater.* **30**, 1900892 (2019).
- [27] E. Puyoo, S. Grauby, J. M. Rampnoux, E. Rouviere, and S. Dilhaire, Thermal exchange radius measurement: application to nanowire thermal imaging, *Rev. Sci. Instrum.* **81**, 073701 (2010).
- [28] X. Liu, S. Li, S. K. Nandi, D. K. Venkatachalam, and R. G. Elliman, Threshold switching and electrical self-oscillation in niobium oxide films, *J. Appl. Phys.* **120**, 124102 (2016).
- [29] S. K. Nandi, S. K. Nath, A. E. El-Helou, S. Li, X. Liu, P. E. Raad, and R. G. Elliman, Current localization and redistribution as the basis of discontinuous current controlled negative differential resistance in NbO_x, *Adv. Funct. Mater.* **29**, 1906731 (2019).
- [30] G. A. Gibson, Designing negative differential resistance devices based on self-heating, *Adv. Funct. Mater.* **28**, 1704175 (2018).
- [31] F. Liu, K. L. Wang, C. Li, and C. Zhou, Study of random telegraph signals in single-walled carbon nanotube field effect transistors, *IEEE Trans. Nanotechnol.* **5**, 441 (2006).
- [32] F. Liu, K. L. Wang, D. Zhang, and C. Zhou, Random telegraph signals and noise behaviors in carbon nanotube transistors, *Appl. Phys. Lett.* **89**, 243101 (2006).
- [33] M. Jerry, K. Ni, A. Parihar, A. Raychowdhury, and S. Datta, Stochastic insulator-to-metal phase transition-based true random number generator, *IEEE Electron Device Lett.* **39**, 139 (2018).
- [34] A. Frenzel, M. M. Qazilbash, M. Brehm, B.-G. Chae, B.-J. Kim, H.-T. Kim, A. V. Balatsky, F. Keilmann, and D. N. Basov, Inhomogeneous electronic state near the insulator-to-metal transition in the correlated oxide VO₂, *Phys. Rev. B* **80**, 115115 (2009).